Published in final edited form as:

Acta Biomater. 2015 November ; 27: 286–293. doi:10.1016/j.actbio.2015.08.045.

Porous titanium bases for osteochondral tissue engineering

Adam B. Nover[a], **Stephanie L. Lee**[a], **Maria S. Georgescu**[a], **Daniel R. Howard**[b], **Reuben A. Saunders**[a], **William T. Yu**[a], **Robert W. Klein**[c], **Anthony P. Napolitano**[c], **Gerard A. Ateshian**[a,d], and **Clark T. Hung**[a]

Adam B. Nover: abn2106@columbia.edu; Stephanie L. Lee: sll2164@columbia.edu; Maria S. Georgescu: sinzigeorgescu@gmail.com; Daniel R. Howard: danhoward@chpnet.org; Reuben A. Saunders: reubens@mit.edu; William T. Yu: wty2102@columbia.edu; Robert W. Klein: Robert.Klein@stryker.com; Anthony P. Napolitano: Napolitano@plymouthcma.com; Gerard A. Ateshian: ateshian@columbia.edu; Clark T. Hung: cth6@columbia.edu

[a]Department of Biomedical Engineering, Columbia University, 351 Engineering Terrace, 1210 Amsterdam Avenue, Mail Code: 8904, New York, NY 10027, USA

[b]Department of Orthopedic Surgery, Mt. Sinai St. Luke's-Roosevelt Hospital, 1000 Tenth Avenue, New York, NY 10019, USA

[c]Stryker Orthopaedics, 325 Corporate Drive, Mahwah, NJ 07430, USA

[d]Department of Mechanical Engineering, Columbia University, 242 S. W. Mudd, 500 West 120th Street, Mail Code: 4703, New York, NY 10027, USA

Abstract

Tissue engineering of osteochondral grafts may offer a cell-based alternative to native allografts, which are in short supply. Previous studies promote the fabrication of grafts consisting of a viable cell-seeded hydrogel integrated atop a porous, bone-like metal. Advantages of the manufacturing process have led to the evaluation of porous titanium as the bone-like base material. Here, porous titanium was shown to support the growth of cartilage to produce native levels of Young's modulus, using a clinically relevant cell source. Mechanical and biochemical properties were similar or higher for the osteochondral constructs compared to chondral-only controls. Further investigation into the mechanical influence of the base on the composite material suggests that underlying pores may decrease interstitial fluid pressurization and applied strains, which may be overcome by alterations to the base structure. Future studies aim to optimize titanium-based tissue engineered osteochondral constructs to best match the structural architecture and strength of native grafts.

Statement of Significance—The studies described in this manuscript follow up on previous studies from our lab pertaining to the fabrication of osteochondral grafts that consist of a bone-like porous metal and a chondrocyte-seeded hydrogel. Here, tissue engineered osteochondral grafts were cultured to native stiffness using adult chondrocytes, a clinically relevant cell source, and a porous titanium base, a material currently used in clinical implants. This porous titanium is manufactured via selective laser melting, offering the advantages of precise control over shape,

Correspondence to: Clark T. Hung, cth6@columbia.edu.

Disclosures

Robert W. Klein and Anthony P. Napolitano are employees of Stryker Orthopaedics and hold stock in the company.

pore size, and orientation. Additionally, this manuscript describes the mechanical influence of the porous base, which may have applicability to porous bases derived from other materials.

Keywords

Tissue engineering; Articular cartilage; Osteochondral grafts; Porous titanium

1. Introduction

Focal defects in articular cartilage caused by acute injury have limited healing capacity and may lead to the progression of joint degradation if untreated [1,2]. Such lesions are common: a systematic review found full-thickness focal defects in 36% of athletes [3]. The most common treatment for large focal defects (>2–3 cm^2) is osteochondral (OC) allografting [2,4,5], the only truly biomimetic technique for restoring tissue organization, which has been used clinically for over 30 years [6] to provide a long-term solution [7]. This treatment is preferred over autografts and autologous chondrocyte implantation (ACI), both of which have been associated with donor site morbidity [8–10]. Additionally, ACI requires multiple stages and is more effective in more active, younger patients [4,9–12].

While OC allografts are preferred as a focal defect treatment, their supply is limited [13,14]. Tissue engineering may provide a cell-based alternative repair strategy, generating additional replacement tissues [15]. We have previously reported on the tissue engineering of articular cartilage grafts that achieve native or near-native mechanical and biochemical properties, using juvenile [16] and adult [11,17] chondrocytes in an agarose hydrogel scaffold system. By integrating this technique with a porous bone or bone-like base, we have engineered osteochondral grafts composed of a viable cell-seeded chondral layer atop the base [11,15,18]. Previous research into the bony base has promoted the use of porous metals, such as tantalum, over devitalized bone [15], with successful evaluation of the metal *in vivo* [11].

Recently a selective laser melting technique was reported to fabricate porous titanium structures for orthopaedic applications [19–21]. Titanium is a corrosion resistant, biocompatible material with a high strength-to-weight ratio [21,22]. The selective laser melting technique offers the valuable ability to select pore size and strut orientation to optimize bone ingrowth (100–700 μm pore size, 60–80% porosity, >50 MPa compression strength) [19,23–28] as well as the potential for fabricating anatomically contoured shapes to match native geometry [29]. A similar process is currently utilized by Stryker Orthopaedics (Mahwah, NJ, USA) to manufacture tibial trays and patellar components for clinical use.

The objective of this study was to adopt and evaluate porous titanium dowels, fabricated through selective laser melting, as a bone-like base for tissue engineered OC constructs using an agarose scaffold system [30–32]. Our investigation focused on characterization of the bases' structure, their influence on measured construct mechanical properties, and their compatibility for viable OC tissue growth.

2. Materials and methods

2.1. Fabrication and structural characterization of porous titanium bases

Cylindrical titanium disks of 4 and 10 mm diameter and 7 mm height were fabricated from commercially pure titanium (Sumitomo, Japan) by Stryker Orthopaedics using an MCP Realizer 2, 250 SLM system (MCP Tooling Technologies, Staffordshire, UK). The system uses an ytterbium fiber laser (600W power CW, $\lambda = 1.06$ μm) with an optical system used to control the movement of the nominal 50 μm diameter focused laser spot on the build area to a positional accuracy of ±5 μm. The system operates in an over pressure argon environment with processing chamber oxygen levels below 0.2%. The atmosphere within the chamber is circulated and filtered to remove process bi-products (titanium nanopowder formed from condensed titanium vapor) from the recycled gas. Parts were built in a layer-wise fashion on a substrate plate connected to an elevator that moves vertically downwards allowing the controlled deposition of powder layers at 50-μm intervals. Upon completion of the build the substrate plate was removed from the build chamber and all un-fused powder was recycled. Test pieces were then cut from the substrate plates. All individual parts were ultrasonically cleaned, dried, and heat treated (1400 °C for 3 h) prior to testing.

Bases were produced with uniform 600, 900, and 1200 μm unit cell pore size with regularly oriented unit cells of struts (0.2 μm thick). Groups are referenced by their unit cell pore size. Representative SEM images have been published by Mullen et al. [19].

As used to characterize trabecular bone, height, diameter, and weight were measured for each construct. Bases were placed in distilled deionized water, degassed, and the submerged weight was measured. From these parameters, the apparent density (ρ) was calculated from the mass and bounding volume. The true density (ρ_s, i.e., density of titanium) was calculated through Archimedes Principle. Metal volume fraction (VF) was calculated as: $VF = \rho/\rho_s$. Porosity (P) was then calculated as $P = 1 - VF = 1 - (\rho/\rho_s)$.

Bases were photographed from the top and side (Fig. 1A) with a stereoscope ($n = 4$). The length of the side of the visible pore square ($n = 6$ pores per base) and strut size ($n = 6$ pores per base) were measured from images using ImageJ (NIH, Bethesda, MD, USA, Fig. 1B). The measured side length was squared to estimate the cross-sectional area of the pore. The images were processed in ImageJ and the pore area fraction was calculated (Fig. 1B).

2.2. Mechanical influence of porous base

Acellular agarose (Type VII, Sigma-Aldrich, St. Louis, MO, USA) disks were cast at 2%, 4%, and 6% w/v of dimensions 4 mmdiameter and 2.3 mm thickness. Agarose disks were mechanically tested using a custom device to acquire the equilibrium Young's modulus (E_Y) at 10% unconfined compressive strain of the disks, as previously described [33]. Each construct was tested twice, once on an impermeable surface (chondral) and once centered on top of a 10 mm diameter titanium disk of 600, 900, and 1200 μm pores (fabricated as previously mentioned) with time in between testing procedures for relaxation (osteochondral). The resulting points for each base type were plotted and fit with a linear regression.

The (on top) testing method was validated by comparing the E_Y of acellular chondral samples tested on top of regularly oriented 1200 μm porous titanium base and of osteochondral samples cast into the porous bases (n = 4–5) where the gel was integrated into the pores. No significant differences (p = 0.73) were observed between the testing configurations, suggesting that the on top test is able to capture the critical features of the gel-pore interactions that influence chondral (region) properties.

The slopes of these regression lines were plotted against their respective unit cell pore size, and the measured pore side length, pore cross-sectional area, pore area fraction, porosity, and apparent density (mean values) for the regularly oriented titanium bases. The appropriate intercept was added when applicable (i.e., a non-porous base would have a porosity of 0). Linear regressions were applied to each plot, and R^2 values were compared.

In order to better understand these results in the context of other types of porous metal bases, this mechanical testing procedure was repeated with randomly oriented 600 μm porous titanium bases [20] and porous tantalum bases (25 mm diameter disk, courtesy Zimmer Biomet, Warsaw, IN, USA) [15], which also show randomly oriented pores (Fig. 2). The apparent density, true density, metal volume fraction, porosity, and pore area fraction were measured as described in Section 2.1. The dimensions of individual pores in these additional bases could not be obtained from image analysis as the pore sizes vary considerably. Note that despite the same unit cell pore size, randomly oriented porous titanium bases contain a higher average pore size than their regular counterparts [20]. When available, the additional measurements of the randomly oriented bases were pooled with those of the regular bases, plotted, and then fitted for correlation purposes.

2.3. Fabrication, culture, and evaluation of cell-seeded OC constructs: viability

Articular cartilage was harvested from adult canine knees 24 h after sacrifice [17,34], then digested in 390 U/mL collagenase type IV (Worthington, Lakewood, NJ, USA) for 8 h with slight agitation. Isolated primary chondrocytes were then passaged twice (P2) in Dulbecco's Modified Eagle's Media (DMEM, Invitrogen, Carlsbad, CA, USA) containing 10% FBS (Atlanta Biologicals, Norcross, GA, USA), 1 ng/mL transforming growth factor-beta-1 (TGF-β1, Invitrogen), 5 ng/mL fibroblast growth factor-2 (FGF-2, Invitrogen), and 1% antibiotics/antimycotics (Invitrogen). Equal volumes of 60×10^6 cells/mL cell suspension and 4% w/v agarose (Type VII, Sigma–Aldrich) were mixed. A custom casting device was manufactured comprised of wells with a ~200 μm lip located 2 mm from the bottom, yielding final parameters of 30×10^6 cells/mL in 2% w/v agarose. OC constructs were cast by filling these wells with cell-seeded agarose, then pressing 4 mm diameter, 600 μm pore size titanium bases into the wells up to the lip, creating constructs with a 2 mm chondral region atop the base with a region of over-lap. Chondral-only controls were cast by filling parallel glass plates with cell-seeded agarose, then punching from this slab, yielding constructs of 4 mm diameter and 2.3 mm thickness.

Constructs were cultured in chemically-defined media consisting of DMEM containing 50 μg/mL L-proline (Sigma–Aldrich), 100 μg/mL sodium pyruvate (Sigma–Aldrich), 1% ITS + premix (BD Biosciences, San Jose, CA, USA), 100 nM dexamethasone (Sigma–Aldrich), 1% antibiotics/antimycotics, 50 μg/mL ascorbic acid (Sigma–Aldrich), and 10 ng/mL

transforming growth factor-beta- 3 (TGF-β3, R&D Systems, Minneapolis, MN, USA) with media changes three times per week for 35 days. Chondral constructs were evaluated at days 0, 14, 28, and 35, and OC constructs were only evaluated at day 35.

At these time points, constructs were evaluated mechanically for E_Y as well as dynamic modulus (G^*), which was evaluated at 0.01 Hz at 1% strain amplitude, superposed over the equilibrated configuration under 10% strain. For OC constructs, interface shear strength was evaluated through destructive testing (schematic shown in Fig. 3). As reported by Lima et al. [15], half of the chondral region was removed with a razor blade. The construct was then clamped in a custom device and aligned with the exposed cross-section parallel to the mechanical tester's impermeable platen. A 10 μm/s linear displacement was applied on the exposed cross-section while load was measured. As in the prior literature [18,35,36], the peak load was reported as the maximum load prior to failure, the shear stiffness was reported as the curve-fit slope of the linear region of the force/displacement curve, and the energy to failure (ETF) was reported as the integrated area under the force/displacement curve up to the failure point, normalized to the interface area.

For biochemical analyses, the chondral region of OC constructs was removed from the base using a razor blade. All constructs were assessed for wet weight (WW) and, after lyophilization, dry weight (DW). They were then digested in 0.5 mg/mL proteinase-K (MP Biomedicals, Santa Ana, CA, USA) for 16 h at 56 °C. DNA content was quantified with a PicoGreen assay (Invitrogen) with lambda phage DNA standards [37]. Glycosaminoglycan (GAG) content was quantified with a 1,9-dimethylmethylene blue (Sigma–Aldrich) dye-binding assay with shark chondroitin-6-sulfate (Sigma– Aldrich) standards [38]. An aliquot of proteinase-K digested solution was hydrolyzed using 12 N HCl at 110 °C for 16 h, then dried, and resuspended in assay buffer [39]. Orthohydroxyproline (OHP) content was then measured by a colorimetric assay for microplates, which involves a reaction between chloramine T and dimethylaminobenzaldehyde. Collagen content was calculated from OHP content by assuming a 1:7.64 OHP-to-collagen mass ratio [40]. These biochemical quantities were analyzed as normalized to WW, DW, and DNA content.

Viability was assessed by halving control constructs or the removed chondral region of OC constructs, staining with a LIVE/DEAD® Assay Kit (Invitrogen), and imaging the cross-section with a confocal microscope (Olympus Fluoview FV1000, Waltham, MA, USA).

For histologic analysis, control constructs and the removed chondral region of OC constructs were fixed in 5% acetic acid, 3.7% formaldehyde, 70% ethanol solution for 24 h, and then stored in 70% ethanol [41]. Fixed samples were serially dehydrated in ethanol, embedded in paraffin (Fisher Scientific, Waltham, MA, USA), and then samples were sectioned to 8 μm and mounted on glass slides. Samples were dewaxed, rehydrated, and stained with Alcian Blue (Sigma–Aldrich) and Picrosirius Red (Sigma–Aldrich) to visualize GAG and collagen distribution, respectively.

2.4. Fabrication, culture, and evaluation of cell-seeded OC constructs: depth-dependent mechanical properties

In addition, another batch of OC and control constructs were cast to the same specifications using P2 juvenile bovine chondrocytes on 600 and 1200 μm bases along with chondral-only control. Constructs were cultured in a similar manner, with media containing PDGF and TGF-β3 supplemented only for the first 14 days [42,43]. At day 35, OC constructs were removed from the bases using a razor blade, and they and chondral-only controls were halved, stained with LIVE/DEAD® Assay Kit (Invitrogen) for contrast, and placed in a custom microscope mounted device. Using this device, 10% compressive strain was applied, and the cross-section was imaged [44,45]. Images were analyzed using texture correlation (Vic-2D, Correlated Solutions) to acquire local strains. The data were minimally cropped to remove edge effects, and then binned into 10 equal regions through the thickness of the construct. For each construct, strains were averaged and normalized by the bin with the most compressive strain (ε_{min}) to facilitate presentation of the strain distribution.

2.5. Statistical analyses

Statistica (Statsoft, Tulsa, OK, USA) was used to perform statistical analyses. One- or Two-way analysis of variance (ANOVA) tests were utilized with a Tukey honest significant difference (HSD) post hoc test ($\alpha = 0.05$) for testing the means ($p \leq 0.05$). For each time point, sample size per group was at minimum three ($n \geq 3$). Regression lines and their statistical comparisons were determined through the method of least squares and regression analysis ($p \leq 0.05$ considered significant) using Microsoft Excel (Redmond, WA, USA). Data are expressed as mean ± standard deviation.

3. Results

Apparent density, volume fraction, porosity, pore side length, and pore area fraction were significantly different ($p \leq 0.001$) for 600, 900, and 1200 μm pore unit cell size groups with minimal variation within groups (Table 1, *unshaded*). For reference, the measured true density (Table 1, *unshaded*) matched that expected of titanium, 4.5 g/cm^3 [46]. There was no significant difference ($p = 0.11–0.99$) in strut thickness across groups. Measured pore side length, strut thickness, and pore area fraction values were similar from top and side views and were pooled with minimal variation.

By simply mechanically testing acellular constructs atop the porous bases, measureable drops in mechanical properties were observed, exacerbated with increasing pore size (Fig. 4 and Table 1). Linear fits ($R^2 > 0.9$) indicated that the apparent E_Y of gel disks tested on 600 μm pore size disks averaged 87% of the true E_Y. This attenuation was 78% for 900 μm and 54% for 1200 μm pore size disks (Fig. 4 and Table 1, *unshaded*). In order to better understand this effect, these characterization processes were repeated with randomly oriented 600 μm pore titanium and tantalum bases, yielding attenuation values of 73% and 85% ($R^2 > 0.9$), respectively (Table 1, *shaded*). Each regression line slope was significant ($p < 0.001$). Slopes for the 1200 μm and tantalum groups are each significantly different from all other groups. The slope for the 900 μm group is not significantly different from that of

either 600 μm group, however the 600 regular and random groups have significantly different slopes ($p < 0.05$).

The slopes obtained from these mechanical tests were correlated with the measured geometric parameters, yielding stronger influence of pore size and area parameters ($R^2 \geq 0.89$) than bulk parameters, such as apparent density and porosity. Adding additional bases to these plots lowered the R^2 values, but maintained the trends (Table 2).

The disparity between gel measured mechanical properties on top of porous bases and gel-alone was caused by the gel bulging/displacing into the base's pores, as visualized by cutting a 10 mm diameter, 1200 μm pore base in half, then using the microscope-mounted device to image a 4% w/v agarose disk (cells added for speckle) compressing into the cut base. By analyzing the area above the struts, it could be seen that there was a decrease in strain magnitude over the pores relative to strut regions (Fig. 5). As this attenuation was lowest using the 600 μm pore bases, this pore size was utilized for the cellular study.

OC constructs cast on 600 μm pore bases grew to 334 ± 86 kPa equilibrium Young's modulus (Fig. 6A), which is in the range of native adult canine tissue (>200 kPa [11]). This was significantly higher than chondral-only controls ($p \leq 0.05$). Dynamic modulus, GAG content, and collagen content were all similar between OC and control constructs (Fig. 6B–D). There were no ostensible differences in construct opacity (Fig. 6E) or cell viability (Fig. 7A) between groups.

Histology (Fig. 7B and C) corroborated biochemical assay data. Staining patterns and intensities were visually similar between control and OC groups for both GAG and collagen stains at day 35. Note that OC groups had been removed from the base prior to fixation, so it is understandable that while the control group shows a dark border of collagen staining around the edges, the OC group shows this pattern around contained edges but not at the gel-base interface.

Destructive shear testing yielded a peak load of 0.63 ± 0.15 N, stiffness of 1.86 ± 0.54 N/mm, and energy to failure of 23.55 J/m^2 describing the gel-base integration strength ($n = 5$).

The measured depth-dependent strain profiles of OC and chondral constructs are presented in Fig. 8. The maximum compressive strain in chondral constructs was located in the construct's crosssectional center, yielding a "U-shape" profile, with the central bins significantly more compliant ($p \leq 0.05$) than the peripheral ones (Fig. 8C). The maximum compressive strain in the OC constructs was located toward where the base was separated, showing significant difference ($p \leq 0.05$) from the distant edge (Fig. 8D and E). Fig. 8F–H visualizes these strain profiles on the constructs.

4. Discussion

In this study, we explored porous titanium as a bone-like base for tissue engineered osteochondral constructs. Here, we displayed the ability to culture titanium-based OC constructs to achieve native levels of the equilibrium Young's modulus (Fig. 6A), using a

clinically relevant adult cell source, as previously done with tantalum-based OC constructs [11,15]. This E_Y and the corresponding biochemical content was similar or higher than that of the chondral-only controls, indicating that, while the titanium struts may block some nutrient transport to the cartilage layer, the inherent beneficial elevation of the cell-seeded hydrogel off the culture dish surface may overcome this effect [47,48]. Additional measurements not reported here confirm repeated ability to grow cartilage tissue on titanium without detriment to cell viability.

The incorporation of the base did not ostensibly alter internal tissue growth patterns. Chondral-only constructs have been shown to grow with a “U-shaped” strain profile across its depth (Fig. 8B, C and F) [45], meaning that the center, where nutrient transport is most limited, is relatively softer than the periphery. Here, OC constructs appeared to have this pattern shifted toward the gel-titanium interface (Fig. 8D and E), implying that the “U-shape” may continue into the overlap region (Fig. 8G and H).

The location of the softest tissue region above the interface could decrease integration between the cartilage and the underlying cartilage. Previously our group had reported integration strength for agarose-tantalum OC constructs grown with juvenile bovine chondrocytes which were comparable with other engineered OCs [36], yet below the native range [15]. The values reported here for titanium-based OC constructs grown with adult canine chondrocytes were slightly lower than those reported for juvenile bovine chondrocytes and tantalum, which is consistent with canine native and engineered tissues being less stiff than corresponding bovine tissues.

Still, the presence of the porous base decreased the cartilage layer’s ability to sustain interstitial fluid pressurization [18], allowing for fluid to exude through the construct’s bottom, where there is generally an impermeable surface during mechanical testing. This is exemplified by the OC constructs’ dynamic modulus (Fig 6B), which, unlike the Young’s modulus, is not higher than that of the control.

Gel penetration into the pores of the underlying substrate (with applied loading) resulted in a lower effective modulus than gels tested on impermeable surfaces (Table 1 and Fig. 4). Correlation analysis indicates that this mechanical effect is a greater function of the size of the pores than of the porosity or density (Table 2). However, as noted from the decrease in correlation due to randomization of the pore structure, it may be difficult to define a single parameter of the porous substrate that is responsible for the attenuated properties of the overlying gel, particularly since many of these descriptive parameters are inherently interrelated. Moreover, parameters such as pore shape, strut geometry, and pore–pore interconnectivity that can be modified in fabrication may also influence the apparent mechanical properties of the composite graft. Nevertheless, this study offers new insights to the complexity of the gel-pore interactions, which may dramatically influence the effective mechanical properties of osteochondral grafts and should be considered in the design of porous bases for this purpose.

We anticipate that with the precise fabrication control offered by the additive manufacturing technique, these negative effects may be minimized with proper structural alterations to the

base. As indicated by the small scatter in the measured properties of porous titanium bases (Table 1), the manufacturing technique allows for precise control of different pore sizes (Table 1), each in the optimal range of porosity reported for bone ingrowth [19], with a titanium volume fraction similar to that of trabecular bone (23.2 ± 5.7% in the femoral neck and 10.7 ± 4.0% in the proximal tibia [49]). Such precision and control over the material fabrication is ideal for fine-tuning of the structure, to optimize both bone integration and engineered cartilage growth in a reproducible manner.

In principle, this additive manufacturing technique could be used to incorporate an impermeable layer separating the gelmetal overlap region from the rest of the base (Fig. 9). This is expected to prevent bulging and increase interstitial pressurization by blocking fluid exudation from the bottom face, thus mimicking the mineralized subchondral plate in the native joint [50]. Such a feature will be especially critical when engineering larger anatomic articular layers, which may not have surrounding tissue to buttress loading of the engineered tissue. Additionally, bases could be fabricated with different pore sizes and orientations above and below the impermeable layer, to independently optimize for osteointegration of the engineered OC graft on the bony side, and cell-seeded gel integration and nutrient transport on the chondral side. Future studies will aim to fabricate, characterize, evaluate *in vitro* and *in vivo*, and optimize titanium-based osteochondral constructs to best mimic native allografts.

5. Conclusions

Porous titanium supports robust cartilage growth, making it a viable bone-like base material for the fabrication of engineered osteochondral tissue constructs, a clinically relevant alternative to allografts. The selective laser melting technique used to fabricate the bases offers exceptional control over the structure of the base. It is anticipated that with this technique, and a better understanding of the physical interaction of the scaffold and tissue of the chondral region with pores of the underlying substrate, porous bases can be tailored to optimize the composite graft's integrative and mechanical properties.

Acknowledgments

This research was supported in part by the National Institutes of Health under award numbers NIH 2R01AR046568, NIH 1R01AR060361, NIH 1S10RR027943, and NIBIB 5P41EB002520. The content is solely the responsibility of the authors and does not necessarily represent the official views of the National Institutes of Health. We thank Stryker Orthopaedics for custom fabricating and donating the titanium bases used in this study. We also thank Rebecca A. Peyser (Columbia University) for helping to prepare histology samples.

References

1. Buckwalter JA, Mankin HJ. Articular cartilage repair and transplantation. Arthritis Rheum. 1998; 41:1331–1342. [PubMed: 9704631]
2. Cole BJ, Pascual-Garrido C, Grumet RC. Surgical management of articular cartilage defects in the knee. J Bone Joint Surg Am. 2009; 91:1778–1790. [PubMed: 19571102]
3. Flanigan DC, Harris JD, Trinh TQ, Siston RA, Brophy RH. Prevalence of chondral defects in athletes' knees: a systematic review. Med Sci Sports Exerc. 2010; 42:1795–1801. [PubMed: 20216470]

4. Sherman SL, Garrity J, Bauer K, Cook J, Stannard J, Bugbee W. Fresh osteochondral allograft transplantation for the knee: current concepts. J Am Acad Orthop Surg. 2014; 22:121–133. [PubMed: 24486758]
5. Gortz S, Bugbee WD. Allografts in articular cartilage repair. J Bone Joint Surg Am. 2006; 88:1374–1384. [PubMed: 16764096]
6. Gross AE, Silverstein EA, Falk J, Falk R, Langer F. The allotransplantation of partial joints in the treatment of osteoarthritis of the knee. Clin Orthop Relat Res. 1975:7–14. [PubMed: 1139838]
7. Gross AE, Shasha N, Aubin P. Long-term followup of the use of fresh osteochondral allografts for posttraumatic knee defects. Clin Orthop Relat Res. 2005:79–87. [PubMed: 15930924]
8. Lee CR, Grodzinsky AJ, Hsu HP, Martin SD, Spector M. Effects of harvest and selected cartilage repair procedures on the physical and biochemical properties of articular cartilage in the canine knee. J Orthop Res. 2000; 18:790–799. [PubMed: 11117302]
9. Reddy S, Pedowitz DI, Parekh SG, Sennett BJ, Okereke E. The morbidity associated with osteochondral harvest from asymptomatic knees for the treatment of osteochondral lesions of the talus. Am J Sports Med. 2007; 35:80–85. [PubMed: 16957009]
10. Whittaker JP, Smith G, Makwana N, Roberts S, Harrison PE, Laing P, et al. Early results of autologous chondrocyte implantation in the talus. J Bone Joint Surg Br. 2005; 87:179–183. [PubMed: 15736739]
11. Ng KW, Lima EG, Bian L, O'Conor CJ, Jayabalan PS, Stoker AM, et al. Passaged adult chondrocytes can form engineered cartilage with functional mechanical properties: a canine model. Tissue Eng Part A. 2010; 16:1041–1051. [PubMed: 19845465]
12. Mandelbaum B, Browne JE, Fu F, Micheli LJ, Moseley JB Jr, Erggelet C, et al. Treatment outcomes of autologous chondrocyte implantation for full-thickness articular cartilage defects of the trochlea. Am J Sports Med. 2007; 35:915–921. [PubMed: 17376858]
13. Paige KT, Vacanti CA. Engineering new tissue: formation of neo-cartilage. Tissue Eng. 1995; 1:97–106. [PubMed: 19877919]
14. Mow VC, Ratcliffe A, Rosenwasser MP, Buckwalter JA. Experimental studies on repair of large osteochondral defects at a high weight bearing area of the knee joint: a tissue engineering study. J Biomech Eng. 1991; 113:198–207. [PubMed: 1875694]
15. Lima EG, Chao PHG, Ateshian GA, Bal BS, Cook JL, Vunjak-Novakovic G, et al. The effect of devitalized trabecular bone on the formation of osteochondral tissue-engineered constructs. Biomaterials. 2008; 29:4292– 4299. [PubMed: 18718655]
16. Mauck R, Soltz M, Wang C, Wong D, Chao PH, Valhmu W, et al. Functional tissue engineering of articular cartilage through dynamic loading of chondrocyte-seeded agarose gels. J Biomech Eng. 2000; 122:9. [PubMed: 10790824]
17. Kelly TAN, Roach BL, Weidner ZD, Mackenzie-Smith CR, O'Connell GD, Lima EG, et al. Tissue-engineered articular cartilage exhibits tensioncompression nonlinearity reminiscent of the native cartilage. J Biomech. 2013; 46:1784–1791. [PubMed: 23791084]
18. Lima EG, Mauck RL, Han SH, Park S, Ng KW, Ateshian GA, et al. Functional tissue engineering of chondral and osteochondral constructs. Biorheology. 2004; 41:577–590. [PubMed: 15299288]
19. Mullen L, Stamp RC, Brooks WK, Jones E, Sutcliffe CJ. Selective laser melting: a regular unit cell approach for the manufacture of porous, titanium, bone in-growth constructs, suitable for orthopedic applications. J Biomed Mater Res Part B. 2009; 89:325–334.
20. Mullen L, Stamp RC, Fox P, Jones E, Ngo C, Sutcliffe CJ. Selective laser melting: a unit cell approach for the manufacture of porous, titanium, bone ingrowth constructs, suitable for orthopedic applications. II. Randomized structures. J Biomed Mater Res Part B. 2010; 92:178–188.
21. Stamp R, Fox P, O'Neill W, Jones E, Sutcliffe C. The development of a scanning strategy for the manufacture of porous biomaterials by selective laser melting. J Mater Sci Mater Med. 2009; 20:1839–1848. [PubMed: 19536640]
22. Santos EC, Osakada K, Shiomi M, Kitamura Y, Abe F. Microstructure and mechanical properties of pure titanium models fabricated by selective laser melting. Proc Inst Mech Eng C-J Mech. 2004; 218:711–719.

23. Kienapfel H, Sprey C, Wilke A, Griss P. Implant fixation by bone ingrowth. J Arthroplasty. 1999; 14:355–368. [PubMed: 10220191]
24. Bobyn JD, Pilliar RM, Cameron HU, Weatherly GC. The optimum pore size for the fixation of porous-surfaced metal implants by the ingrowth of bone. Clin Orthop Relat Res. 1980:263–270. [PubMed: 7428231]
25. Bobyn JD, Stackpool GJ, Hacking SA, Tanzer M, Krygier JJ. Characteristics of bone ingrowth and interface mechanics of a new porous tantalum biomaterial. J Bone Joint Surg Br. 1999; 81:907–914. [PubMed: 10530861]
26. Niles JL, Coletti JM Jr, Wilson C. Biomechanical evaluation of bone-porous material interfaces. J Biomed Mater Res. 1973; 7:231–251. [PubMed: 4703760]
27. Hulbert SF, Young FA, Mathews RS, Klawitter JJ, Talbert CD, Stelling FH. Potential of ceramic materials as permanently implantable skeletal prostheses. J Biomed Mater Res. 1970; 4:433–456. [PubMed: 5469185]
28. Assad M, Jarzem P, Leroux MA, Coillard C, Chernyshov AV, Charette S, et al. Porous titanium-nickel for intervertebral fusion in a sheep model: Part 1. Histomorphometric and radiological analysis. J Biomed Mater Res Part B. 2003; 64:107–120.
29. Hung CT, Lima EG, Mauck RL, Takai E, LeRoux MA, Lu HH, et al. Anatomically shaped osteochondral constructs for articular cartilage repair. J Biomech. 2003; 36:1853–1864. [PubMed: 14614939]
30. Benya PD, Shaffer JD. Dedifferentiated chondrocytes reexpress the differentiated collagen phenotype when cultured in agarose gels. Cell. 1982; 30:215–224. [PubMed: 7127471]
31. Selmi T, Neyret P, Verdonk PCM, Barnouin L. Autologous chondrocyte transplantation in combination with an alginate-agarose based hydrogel (Cartipatch). Tech Knee Surg. 2007; 6:253–258.
32. Duan X, Zhu X, Dong X, Yang J, Huang F, Cen S, et al. Repair of large osteochondral defects in a beagle model with a novel type I collagen/ glycosaminoglycan-porous titanium biphasic scaffold. Mater Sci Eng C. 2013; 33:3951–3957.
33. Soltz MA, Ateshian GA. Experimental verification and theoretical prediction of cartilage interstitial fluid pressurization at an impermeable contact interface in confined compression. J Biomech. 1998; 31:927–934. [PubMed: 9840758]
34. Bian L, Fong JV, Lima EG, Stoker AM, Ateshian GA, Cook JL, et al. Dynamic mechanical loading enhances functional properties of tissue-engineered cartilage using mature canine chondrocytes. Tissue Eng Part A. 2010; 16:1781–1790. [PubMed: 20028219]
35. Broom ND, Oloyede A, Flachsmann R, Hows M. Dynamic fracture characteristics of the osteochondral junction undergoing shear deformation. Med Eng Phys. 1996; 18:396–404. [PubMed: 8818138]
36. Allan K, Pilliar R, Wang J, Grynpas M, Kandel R. Formation of biphasic constructs containing cartilage with a calcified zone interface. Tissue Eng. 2007; 13:167–177. [PubMed: 17518590]
37. McGowan K, Kurtis M, Lottman L, Watson D, Sah R. Biochemical quantification of DNA in human articular and septal cartilage using PicoGreen® and Hoechst 33258. Osteoarthr Cartilage. 2002; 10:580–587.
38. Farndale RW, Sayers CA, Barrett AJ. A direct spectrophotometric microassay for sulfated glycosaminoglycans in cartilage cultures. Connect Tissue Res. 1982; 9:247–248. [PubMed: 6215207]
39. Stegemann H, Stalder K. Determination of hydroxyproline. Clin Chim Acta. 1967; 18:267–273. [PubMed: 4864804]
40. Hollander AP, Heathfield TF, Webber C, Iwata Y, Bourne R, Rorabeck C, et al. Increased damage to type II collagen in osteoarthritic articular cartilage detected by a new immunoassay. J Clin Invest. 1994; 93:1722–1732. [PubMed: 7512992]
41. Lin W, Shuster S, Maibach HI, Stern R. Patterns of hyaluronan staining are modified by fixation techniques. J Histochem Cytochem. 1997; 45:1157– 1163. [PubMed: 9267476]
42. Lima EG, Bian L, Ng KW, Mauck RL, Byers BA, Tuan RS, et al. The beneficial effect of delayed compressive loading on tissue-engineered cartilage constructs cultured with TGF-beta3. Osteoarthr Cartilage. 2007; 15:1025–1033.

43. Ng KW, O'Conor CJ, Kugler LE, Cook JL, Ateshian GA, Hung CT. Transient supplementation of anabolic growth factors rapidly stimulates matrix synthesis in engineered cartilage. Ann Biomed Eng. 2011; 39:2491–2500. [PubMed: 21833681]
44. Wang CC, Chahine NO, Hung CT, Ateshian GA. Optical determination of anisotropic material properties of bovine articular cartilage in compression. J Biomech. 2003; 36:339–353. [PubMed: 12594982]
45. Kelly TA, Ng KW, Wang CC, Ateshian GA, Hung CT. Spatial and temporal development of chondrocyte-seeded agarose constructs in free-swelling and dynamically loaded cultures. J Biomech. 2006; 39:1489–1497. [PubMed: 15990101]
46. Haynes, WM. CRC Handbook of Chemistry and Physics. CRC Press; 2013.
47. Bian L, Angione SL, Ng KW, Lima EG, Williams DY, Mao DQ, et al. Influence of decreasing nutrient path length on the development of engineered cartilage. Osteoarthr Cartilage. 2009; 17:677–685.
48. Cigan AD, Nims RJ, Albro MB, Vunjak-Novakovic G, Hung CT, Ateshian GA. Nutrient channels and stirring enhanced the composition and stiffness of large cartilage constructs. J Biomech. 2014; 47:3847–3854. [PubMed: 25458579]
49. Liu XS, Sajda P, Saha PK, Wehrli FW, Bevill G, Keaveny TM, et al. Complete volumetric decomposition of individual trabecular plates and rods and its morphological correlations with anisotropic elastic moduli in human trabecular bone. J Bone Miner Res. 2008; 23:223–235. [PubMed: 17907921]
50. Hwang J, Bae WC, Shieu W, Lewis CW, Bugbee WD, Sah RL. Increased hydraulic conductance of human articular cartilage and subchondral bone plate with progression of osteoarthritis. Arthritis Rheum. 2008; 58:3831– 3842. [PubMed: 19035476]

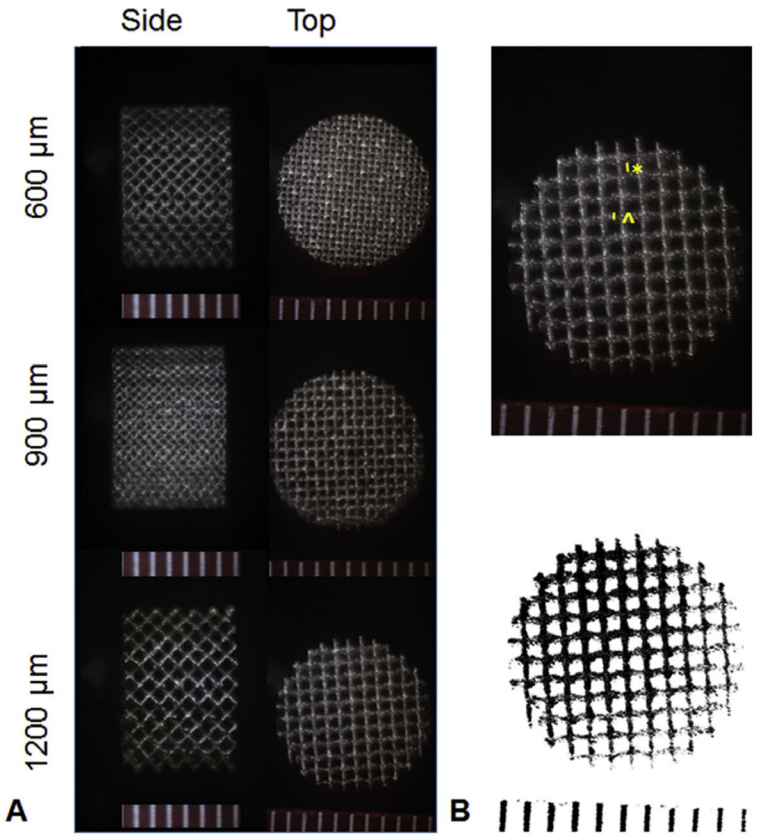

Fig. 1.

(A) Representative stereoscopic images of 10 mm porous titanium disks with uniform pore distribution; (B) *Top:* Strut thickness (^) and pore side length (*) shown on a 1200 µm unit cell pore size base; *Bottom:* The same base processed for area fraction measurements. Scale bars in mm.

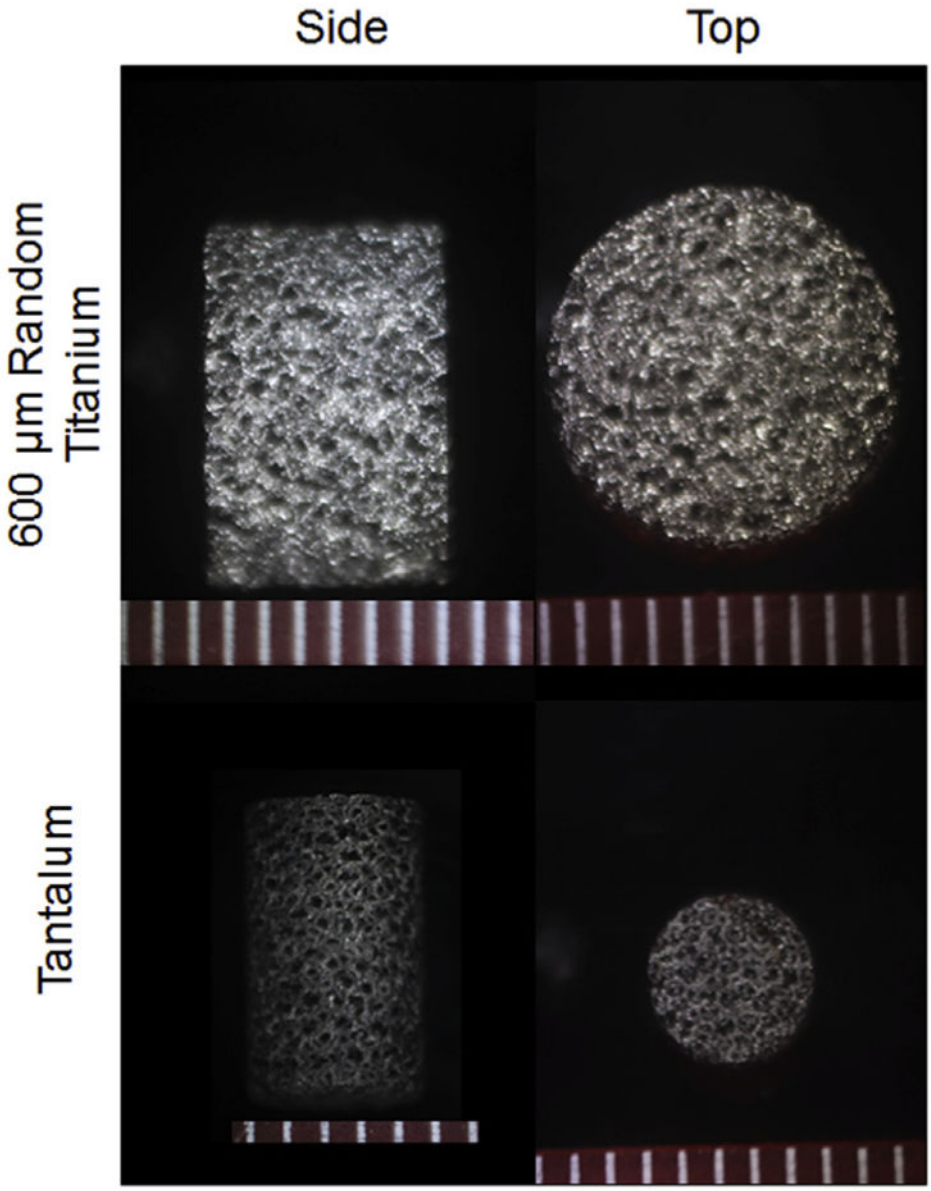

Fig. 2.

Representative stereoscopic images of 10 mm diameter 600 µm randomly oriented porous titanium and 4.7 mm diameter porous tantalum. Scale bars in mm.

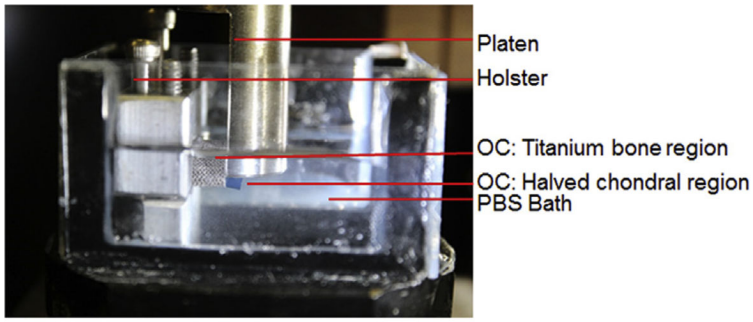

Fig. 3.

Annotated photo of shear testing apparatus with gel contrast enhanced in blue for visualization.

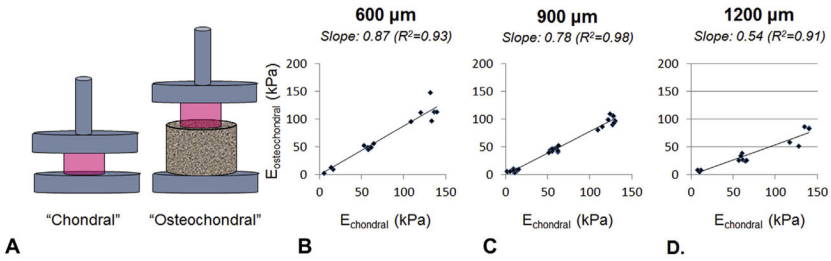

Fig. 4.

(A) Schematic: mechanically testing E_Y of acellular agarose hydrogels on an impermeable surface ($E_{chondral}$, *left*) and atop a porous titanium base ($E_{osteochondral}$, *right*). Relationship between $E_{chondral}$ and $E_{osteochodnral}$ using (B) 600; (C) 900; (D) and 1200 μm pore bases using 2%, 4%, 6% w/v agarose. Curve-fit slopes ($R_2 > 0.9$) are indicated above graphs. For each scatterplot, $n \geq 14$.

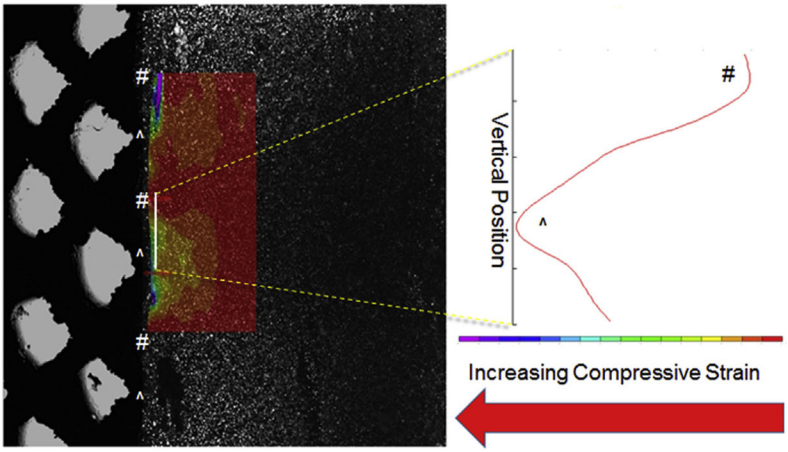

Fig. 5.

A representative composite of transmitted light and fluorescent light images, showing 4% agarose gel compressed against a cut 1200 μm pore titanium base (20% applied strain, cells seeded for speckle) with overlaid compressive strain map (*left*). Open pores abutting gel are marked with # and struts abutting gel are marked with ^. Compressive strain across the solid white line plotted (*right*) indicating increased compressive strain over struts (^) compared to pores (#).

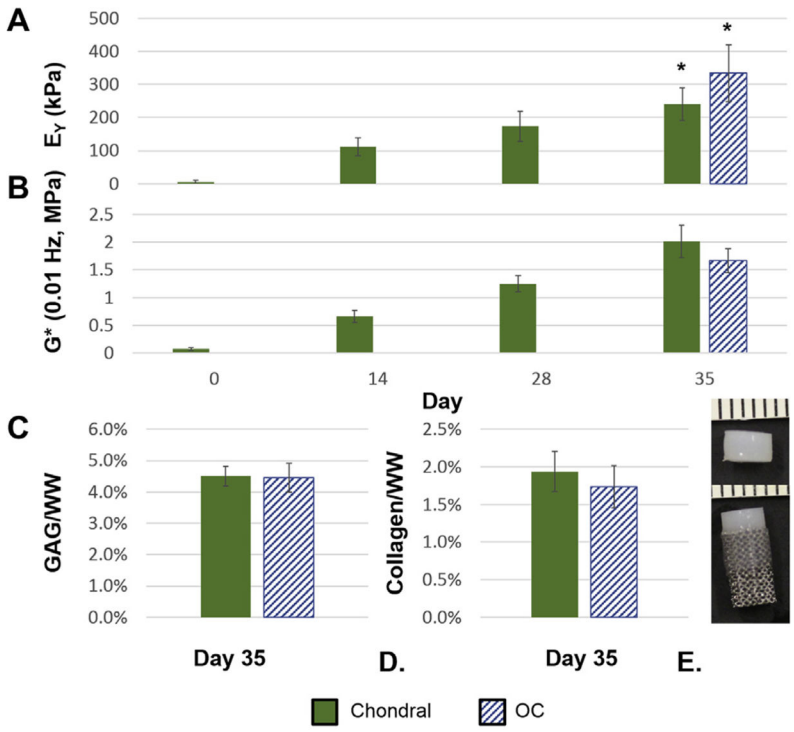

Fig. 6.

(A) Equilibrium Young's modulus (E_Y); (B) and dynamic modulus (G^*) measured at 0.01 Hz across days 0, 14, 28, and 35 (n = 3–4 for days 0, 14, 28; n = 8 for day 35); (C) glycosaminoglycan content per wet weight (GAG/WW); (D) and collagen content per wet weight (Collagen/WW) at day 35 ($n \geq 7$); (E) construct photos (chondral, *top*; osteochondral, *bottom*) at day 35. Data are expressed as mean ± standard deviation. Indicates significantly different groups ($p \leq 0.05$).

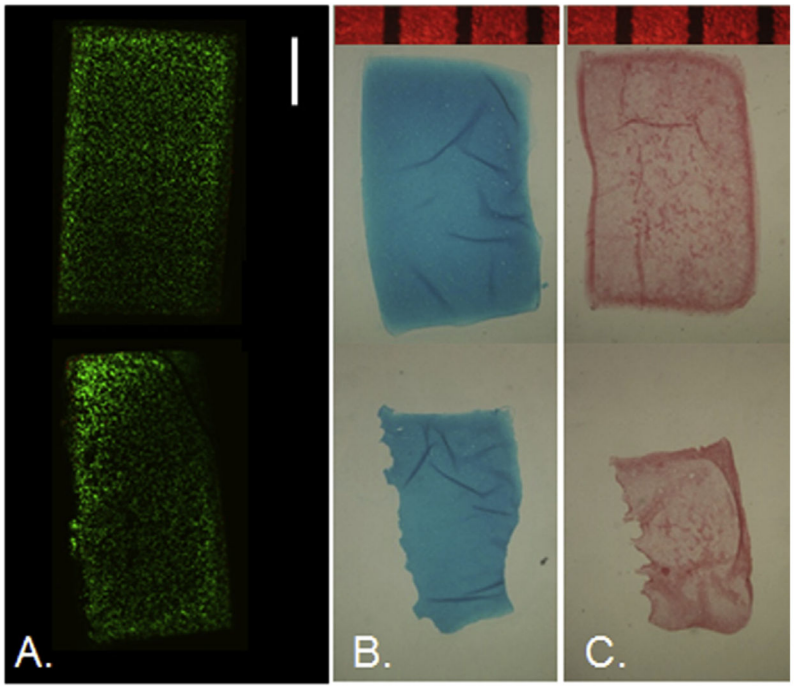

Fig. 7.

Day 35 representative cross-sectional images for (A) live/dead (n = 1), (B) Alcian blue (n = 3), and (C) Picrosirius red (n = 3) staining for chondral-only control (top) and osteochondral (bottom) constructs. OC constructs are positioned with the gel's top surface facing right. Scale bar indicates 1 mm.

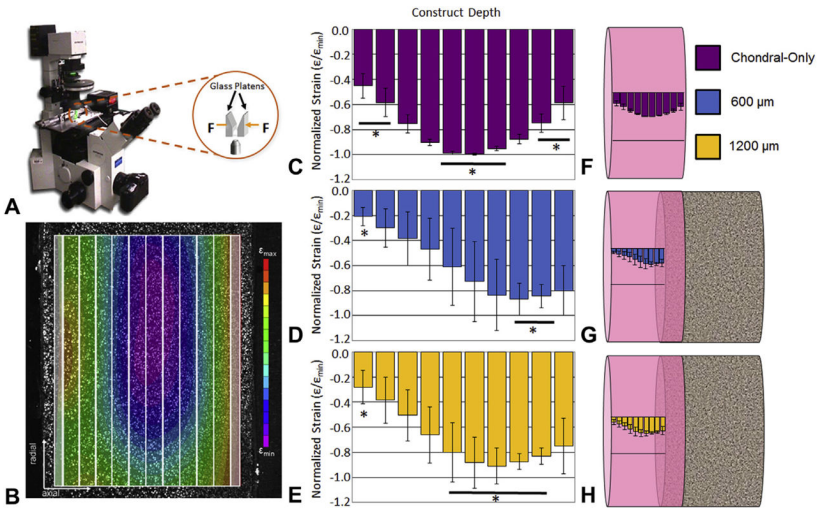

Fig. 8.

(A) Schematic of microscope-mounted depth-dependent testing setup, adapted from [44]. (B) Representative strain map of control construct showing "U-shape" profile with bins demarcated. Average strain profiles normalized by peak compressive strain for (C) chondral-only controls; and for osteochondral constructs grown on (D) 600; and (E) 1200 μm pore bases. Indicates significantly different groups ($p \leq 0.05$). For each group, $n = 3–4$. (F and G) Respective average strain profiles contextualized on schematics of chondral-only and osteochondral constructs. Data are expressed as mean ± standard deviation.

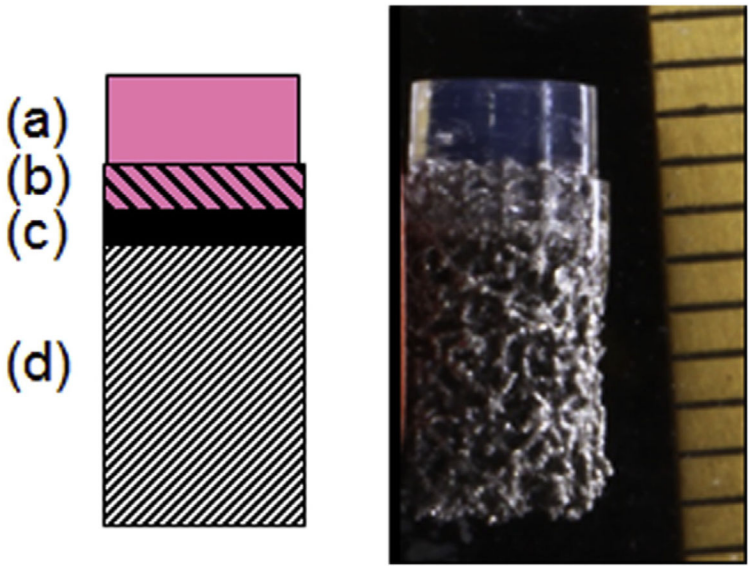

Fig. 9.

Schematic (*left*) and gross photo (*right*) of an OC construct with a multilayered bases consisting of a cell-seeded chondral region (a), a gel-integrating region (b), an impermeable interface (c), and a bone-integrating region (d).

Table 1

(*Unshaded*) Properties of regularly oriented 600, 900, and 1200 μm porous titanium bases: Apparent density (n = 11–12); true density (i.e., density of titanium or tantalum, n = 11–12); metal volume fraction (n = 11–12); porosity (n = 11–12), pore side length (n = 6 pores per 4 bases per top and side), strut thickness (n = 6 pores per 4 bases per top and side); and pore area fraction (n = 4–6 per top and side). (*Shaded*) Properties of additional bases: randomly oriented 600 μm porous titanium (n = 11–12 for apparent density, true density, metal volume fraction, and porosity; n = 4 per top and side for pore area fraction) and porous tantalum (n = 6 for apparent density, true density, metal volume fraction, and porosity; n = 4 per top and side for pore area fraction). Data are expressed as mean ± standard deviation. Letters indicate significantly different groups ($p \leq 0.001$). The final column summarizes obtained the linear regression value and R_2 obtained from testing acellular samples on bases or on an impermeable platen (see Fig. 4). Slopes for 600-random and tantalum groups stem from n = 15 to n = 9 points, respectively. Each linear regression slope is significant ($p < 0.001$). Slopes for the 1200 μm and tantalum groups are each significantly different from all other groups. The slope for the 900 μm group is not significantly different from that of either 600 μm group, however the 600 regular and random groups have significantly different slopes ($p < 0.05$).

Group	Unit Cell Pore Size (μm)	Apparent Density (g/cm^3)	True Density (g/cm^3)	Metal Volume Fraction	Porosity	Pore Side Length (mm)	Pore Cross-sectional Area (mm^2)	Strut Thickness (mm)	Pore Area Fraction	$E_{osteochondral}/E_{chondral}$ Slope
600-Regular	600	1.59±0.03^A	4.34±0.12^A	0.37±0.01^A	0.63±0.01^A	0.25±0.03^A	0.65±0.01^A	0.18±0.02	0.26±0.03^A	0.87, R^2=.93
900-Regular	900	0.78±0.02^B	4.28±0.21^A	0.18±0.01^B	0.82±0.01^B	0.44±0.03^B	0.20±0.02^B	0.18±0.02	0.42±0.04^B	0.78, R^2=0.98
1200-Regular	1200	0.45±0.02^c	4.47±0.49^A	0.10±0.01^c	0.90±0.01^c	0.64±0.04^c	0.41±0.05^c	0.18±0.01	0.54±0.03^c	0.54, R^2=.91
600-Random	600	1.56±0.03^A	4.30±0.13^A	0.36±0.01^A	0.64±0.01^A	N/A	N/A	N/A	0.26±0.02^A	0.73, R^2=0.96
Tantalum	N/A	3.96±0.18^D	14.7±1.6^B	0.27±0.03^D	0.73±0.03^D	N/A	N/A	N/A	0.29±0.06^A	0.85, R^2=0.96

Table 2

Goodness of fit (R_2) for regression lines from plots of the $E_{ostechondral}/E_{chondral}$ slope values as a function of listed parameters (mean values) including only regularly oriented 600, 900, and 1200 μm porous titanium bases (*left*) or including regularly oriented 600, 900, and 1200 μm porous titanium, randomly oriented 600 μm porous titanium, and porous tantalum (*right*). As the unit cell pore size for tantalum was not known, it was not included in this plot. Pore side length could not be measured for either randomly oriented structure, so no additional plots could be made for related parameters (marked "N/A").

Parameter	R^2	
	Regular bases only	**All bases**
Unit cell pore size (μm)	0.89	0.83
Apparent density (g/cm^3)	0.78	0.55
Metal volume fraction	0.71	0.53
Porosity	0.71	0.53
Pore side length (mm)	0.94	N/A
Pore cross-sectional area (mm^2)	0.98	N/A
Pore area fraction	0.93	0.89